PNAS RESEARCH ARTICLE | MEDICAL SCIENCES OPEN ACCESS

Extracellular vesicles from triple negative breast cancer promote pro-inflammatory macrophages associated with better clinical outcome

Mercedes Tkach[a,1], Jessie Thalmensi[a], Eleonora Timperi[a], Paul Gueguen[a], Nathalie Névo[a], Eleonora Grisard[a], Philemon Sirven[a], Federico Cocozza[a], Alizée Gouronnec[a], Lorena Martin-Jaular[a], Mabel Jouve[b], Fabien Delisle[a], Nicolas Manel[a], Derek C. Rookhuizen[a], Coralie L. Guerin[c,d], Vassili Soumelis[e,f], Emanuela Romano[a], Elodie Segura[a], and Clotilde Théry[a,1]

Edited by Myles Brown, Dana-Farber Cancer Institute, Boston, MA; received April 23, 2021; accepted March 14, 2022

Tumor associated macrophages (TAMs), which differentiate from circulating monocytes, are pervasive across human cancers and comprise heterogeneous populations. The contribution of tumor-derived signals to TAM heterogeneity is not well understood. In particular, tumors release both soluble factors and extracellular vesicles (EVs), whose respective impact on TAM precursors may be different. Here, we show that triple negative breast cancer cells (TNBCs) release EVs and soluble molecules promoting monocyte differentiation toward distinct macrophage fates. EVs specifically promoted proinflammatory macrophages bearing an interferon response signature. The combination in TNBC EVs of surface CSF-1 promoting survival and cargoes promoting cGAS/STING or other activation pathways led to differentiation of this particular macrophage subset. Notably, macrophages expressing the EV-induced signature were found among patients' TAMs. Furthermore, higher expression of this signature was associated with T cell infiltration and extended patient survival. Together, this data indicates that TNBC-released CSF-1-bearing EVs promote a tumor immune microenvironment associated with a better prognosis in TNBC patients.

extracellular vesicles | exosomes | macrophages | triple-negative breast cancer | CSF-1

Significance

Our work uncovers mechanisms by which tumor cells impact tumor-associated macrophages in human triple-negative breast cancer. Via extracellular vesicles (EVs), these tumors promote macrophages with proinflammatory features, correlated with better clinical outcome. Our results suggest exploration of these EVs as tools, alone, or in combination with other therapies, to promote a favorable environment for the generation of anti-tumor immune responses.

Tumors are infiltrated by different populations of immune cells, macrophages, in particular, being major components of the tumor microenvironment. Tumor-associated macrophages (TAMs) favor tumor progression, promoting cancer cell invasion and metastasis in mouse models (1). Recent single-cell analyses of human cancers revealed the heterogeneity of macrophage populations, thus challenging our understanding of TAM biology (2–4). TAMs derive from circulating monocytes that are recruited into the tumor via the CCL2-CCR2 chemokine signaling pathway (5, 6). The fate of monocytes is not predetermined and largely depend on the microenvironmental cues they encounter (7). Specifically, the identity of tumor-derived factors that contribute to TAM heterogeneity and the mechanisms underlying intratumoral monocyte differentiation remain unclear.

Among the signals that can impact TAM differentiation and activation, cytokines and chemokines are well-characterized factors (8); extracellular vesicles (EVs), however, represent novel candidates. EVs are complex vehicles of intercellular communication and were suggested to have an impact on macrophage activation (9–12). EVs, such as exosomes, ectosomes, microvesicles, and oncosomes, are membrane-enclosed structures that contain proteins and nucleic acids and can be released into the extracellular environment by all cell types, including cancer cells (13, 14). Once released, EVs can interact with recipient cells and modulate their function (15). Particularly, EVs released by cancer cells play an important role in shaping the tumor immune microenvironment. EVs were shown to modulate lymphocytes and myeloid cell functions in cancer by triggering either protumor or anti-tumor immune responses (16, 17), which may depend on numerous factors, such as the cancer type, stage, or EV subtype analyzed (18). Here, we address the specific contribution of tumor-derived EVs, as compared to the tumor-derived soluble factors, in driving TAM heterogeneity. For this, we focus on human breast cancer since these tumors are highly infiltrated with macrophages (1). Our results confirm a striking functional difference of EVs and soluble factors in tuning TAM profile that we attribute to the combination of survival and activation signals carried by EVs. Furthermore, we unravel an unexpected ability of TNBC-EVs to promote an inflammatory tumor microenvironment associated with a better clinical outcome.

Author affiliations: [a]INSERM U932, Institut Curie, PSL Research University, 75005, Paris, France; [b]CNRS UMR3215, Institut Curie, PSL Research University, 75005, Paris, France; [c]Cytometry Platform, CurieCoreTech, Institut Curie, Paris, F-75005 France; [d]Innovative Therapies in Haemostasis, INSERM, Université de Paris, Paris, F-75006 France; [e]Université de Paris, Inserm, U976 HIPI Unit, F-75006, Paris, France; and [f]Assistance Publique-Hôpitaux de Paris (AP-HP), Laboratoire d'Immunologie et Histocompatibilité, Hôpital Saint-Louis, F-75010, Paris, France

Author contributions: M.T., E.S., and C.T. designed research; M.T., J.T., E.T., N.N., E.G., P.S., F.C., A.G., L.M.-J., M.J., F.D., and C.L.G. performed research; P.G., P.S., N.M., D.C.R., V.S., and E.R. contributed new reagents/analytic tools; M.T., J.T., E.T., P.G., N.N., E.G., P.S., F.C., A.G., L.M.-J., M.J., F.D., N.M., C.L.G., E.S., and C.T. analyzed data; and M.T., E.S., and C.T. wrote the paper.

The authors declare no competing interest.

This article is a PNAS Direct Submission.

[1]To whom correspondence may be addressed. Email: mercedes.tkach@gmail.com or clotilde.thery@curie.fr.

This article contains supporting information online at http://www.pnas.org/lookup/suppl/doi:10.1073/pnas.2107394119/-/DCSupplemental.

Published April 19, 2022.

Results

Efficient Separation of EVs from Soluble Factors by Size Exclusion Chromatography. While analyzing EVs from a triple negative breast cancer cell (TNBC) cell line interacting with human immune cells, we have observed a major targeting of these EVs to monocytes (*SI Appendix*, Fig. 1), suggesting a possible downstream action of EVs on monocyte differentiation. For this experiment, EVs had been obtained by a crude process of differential ultracentrifugation of the cell conditioned medium (CM), known to coisolate other nonvesicular components (19). To minimize the level of soluble proteins coisolated with EVs, and thus be able to evaluate the specific impact of cancer cell derived EVs on monocyte fate, we implemented a sequential purification protocol (20). CM of MDA-MB-231 tumor cells was concentrated by ultrafiltration using 100 kDa MWCO filter, followed by size exclusion chromatography (SEC) (Fig. 1*A*). This enabled us to efficiently separate the components present in the preconcentrated CM (CCM) (Fig. 1 *A* and *B*). EVs eluted in fractions 8–10, as evidenced by the high concentration of particles measured by Nanoparticle Tracking Analysis (NTA), whereas protein concentration increased from fraction 12 onwards and peaked after fraction 17 (Fig. 1*B* and total protein gel in Fig. 1*C*). To characterize the eluted vesicles, we performed Western blot analysis on all the collected SEC fractions and evaluated the presence of classical EV markers. Most particles eluted before F10 (Fig. 1*B*), and the EV markers CD63 and CD9 were observed mainly in F8–F11 and F8–F9 for CD63 and CD9, respectively; however, we note that both were also detected at lower levels up to F17–19 (Fig. 1*C*). Similarly, the EV-specific marker HSC70 was only eluted in the first fractions (up to F10), whereas Syntenin-1, which is also associated with EVs, was present from F8 up to F17. Another marker recently attributed to non-exosomal small EVs (21), 14-3-3 protein, appeared in the late SEC fractions, thus, not associated with the EV-specific markers (Fig. 1*C*). Further visualization of the pooled EV SEC fractions using transmission electron microscopy (TEM) with negative staining confirmed that early fractions (F7–F10) contained a mixture of cup-shaped EVs of 80–100 nm, together with smaller round structures of 30–40 nm (Fig. 1 *C*, *Lower Part*). Conversely, late SEC fractions (F15–F22) lacked EVs as well as these smaller structures and were enriched in electron-dense particles smaller than 25 nm (Fig. 1*C*). Finally, interleukin (IL)-6 and IL-8, two cytokines known to be secreted by MDA-MB-231, were detected from F13 onward, with higher amounts in F17 and later fractions (Fig. 1*D*). Collectively, these results demonstrate the suitability of SEC to isolate EV-rich (EV-R: F7–F10) and EV-poor (EV-P: F15–F22) fractions (Fig. 1*C*).

We next analyzed the MDA-MB-231-EV-R surface signature using a bead-based assay based on the capture of EVs on antibody-coated beads, which are subsequently detected by flow-cytometry using a combination of three antibodies against CD9, CD81, and CD63 tetraspanins (TSPs) (MACSPlex Exosome) (22). Among the 37 surface markers analyzed in this

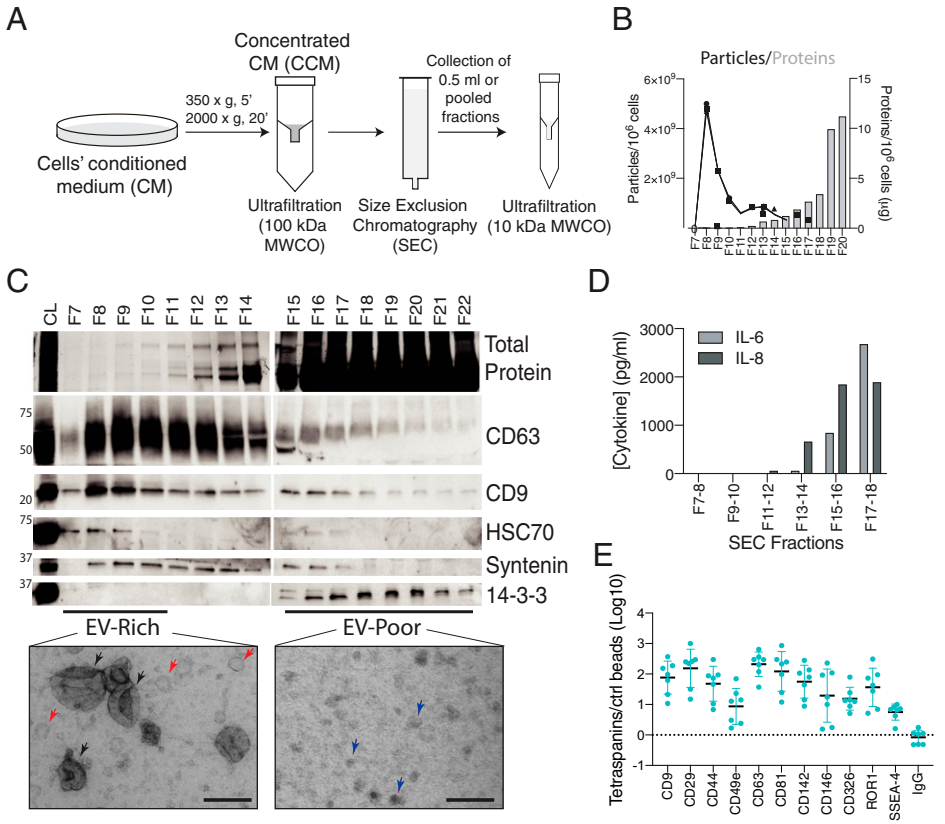

Fig. 1. Efficient separation of MDA-MB-231-derived secretome into EVs and soluble factors by ultrafiltration and SEC. (*A*) Scheme of collection of the EV-enriched and EV-poor fractions. Conditioned medium from MDA-MB-231 cells cultured ON in serum free medium was concentrated by ultrafiltration with 100 KDa cutoff filters. 0.5 mL of the concentrated conditioned medium (CCM) was subjected to size exclusion chromatography, and 0.5 mL individual or pooled fractions were collected and concentrated using 10 KDa cutoff filters. (*B*) Vesicle count and protein quantification on individual fractions is shown. Representative of two independent experiments. (*C*) WB of EV-associated proteins done on individual fractions and transmission electron microscopy of the pooled EV-rich (EV-R) and EV-poor (EV-P) fractions. (Scale bar: 100 nm.) Representative of three independent experiments. (*D*) Quantification of IL-6 and IL-8 present in pooled SEC fractions from MDA-MB-231 cells. Representative of two independent experiments. (*E*) MACSPlex Exosome on EV-containing fractions (F7-10) developed using a mix of antibodies against TSPs (CD9, CD63, and CD81). Results for individual EV isolations are shown ($n = 7$).

assay, MDA-MB-231 EVs expressed the TSPs CD9, CD63, and CD81, the sialylated glycolipid SSEA-4, several receptors for signaling molecules: ROR1 (receptor for Wnt5a), CD44 (heparan sulfate proteoglycan that can bind cytokines), and CD142 (*F3*, tissue factor = initiator of coagulation), and several molecules mediating adhesion to other cells or to extracellular matrix: integrins CD29 (*ITGB1*) and CD49e (*ITGA5*), and cell adhesion molecules CD146 (*MCAM*) and CD326 (*EPCAM*) (Fig. 1*E*). This complex array of surface molecules could therefore confer EVs a particular way of interacting with their environment, different from the way soluble proteins interact with their targets via a single receptor.

TNBC-Derived EVs and Soluble Factors Induce Monocyte Differentiation Toward Macrophages. Blood monocytes are plastic cells that can be recruited to tissues during inflammation, giving rise to monocyte-derived (mo-derived) cells, such as TAMs. To evaluate the role of EVs and soluble factors released by tumors in monocyte activation and differentiation, we incubated human blood $CD14^+$ monocytes with MDA-MB-231 tumor cell-derived EV-R or EV-P fractions. In both cases, a higher number of mo-derived cells after 5 d of culture were obtained, as compared to untreated monocytes (Fig. 2*A*). Human monocytes do not proliferate in vitro, thus, our results suggest that SEC fractions promote monocyte survival. Notably, the increased survival was comparable to that observed when monocytes were cultured with essential myeloid growth factors (23), recombinant macrophage-colony-stimulating factor (M-CSF = CSF-1, gene *CSF1*) or granulocyte-macrophage CSF (GM-CSF, gene *CSF2*) (Fig. 2*A*). Furthermore, phenotypic characterization of these mo-derived cells revealed a typical macrophage morphology for EV-R-, EV-P-, and CSF-1-treated monocytes, while this was slightly less evident for GM-CSF-activated monocytes (Fig. 2*B*). Classical macrophage surface markers, such as CD68 and MERTK (Fig. 2*C*), were readily detected in all the mo-derived cells. However, we observed differences in their expression levels between mo-derived macrophages (mo-macs) exposed to EV-R (EV-R-mo-macs) or EV-P (EV-P-mo-macs) fractions (Fig. 2*C* and *SI Appendix*, Fig. 2*A*). Notably, EV-R-mo-macs expressed higher levels of CD163, MERTK, CD88, CD204, and PD-L1 and lower levels of the mannose receptor (MRC1/CD206) compared to EV-P-mo-macs (Fig. 2*C*).

Because TAMs coexpress high levels of CD206 and CD163, we decided to focus on the number of live mo-derived cells that expressed these two markers upon EV-R or EV-P in vitro stimulation (Fig. 2*D*). When compared to macrophages differentiated in vitro with recombinant cytokines, we observed that expression of these markers on EV-R-mo-macs resembled that of CSF-1-induced mo-macs, while EV-P-mo-macs were more similar to the mo-derived cells generated by GM-CSF

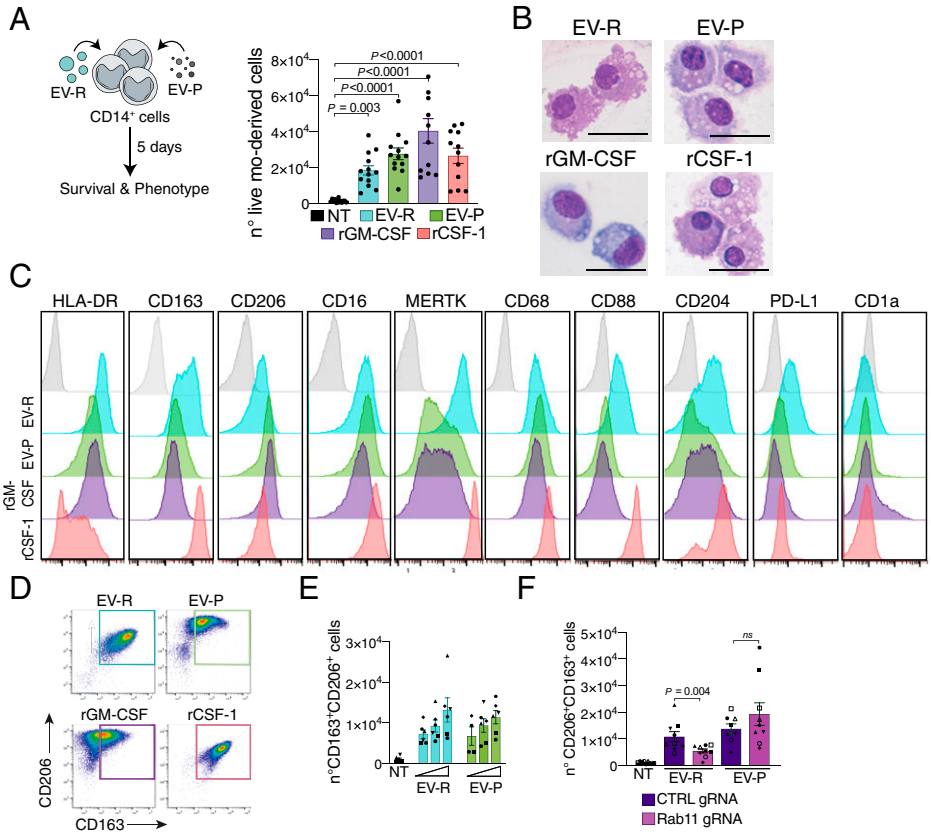

Fig. 2. EVs and soluble factors from MDA-MB-231 cells promote the differentiation of monocytes toward macrophages. (*A*) Equal amount of proteins (4 μg) from pooled EV-R (F7–F10) or EV-poor (F15–F22) fractions were incubated for 5 d with freshly isolated $CD14^+$ monocytes from healthy donors in the absence of any other stimuli. As control, $CD14^+$ cells were also incubated with 100 ng/mL of rCSF-1 or rGM-CSF. On day 5, live cells were counted on each well by flow cytometry. (*B*) Mo-derived cells morphology was analyzed by cytospin at the end of the culture (Day 5). (Scale bars: 30 μm.) Representative of two independent experiments. (*C*) Analysis of macrophage marker expression by flow cytometry. Representative of two (for CD68, CD88, and CD1a expression) and of three to ten independent donors for the other markers (isotype control on CSF-1-treated cells is shown in gray). (*D*) CD206 vs. CD163 density plot of cells at day 5. Representative of four independent experiments. (*E*) Quantification of $CD206^+CD163^+$ live macrophages on day 5 of culture of monocytes with increasing doses of each pooled fraction (0.5, 1, and 2 μg of proteins). (*F*) Quantification of $CD206^+CD163^+$ live macrophages on day 5 of culture of monocytes with EV-R or EV-P fractions from equal numbers of control (CTRL gRNA) or Rab11a-KO (Rab11 gRNA) MDA-MB-231 cells. Each individual donor is shown (n = 9). Comparison between groups was performed by two-tailed, Wilcoxon test. P values ≤0.05 were considered significant and are indicated for each comparison. Each individual donor is shown. Results shown represent mean ± SEM.

(Fig. 2*D*). Finally, the number of $CD206^+CD163^+$ mo-macs recovered at the end of the culture was dependent on the amount of EV-R or EV-P (Fig. 2*E*).

To directly test the role of EVs in macrophage differentiation, we depleted Rab11a by CRISPR/Cas9 as this protein was proposed to be required for the release of EVs (24, 25). Consistent with observations in other cell types, depletion of Rab11 by CRISPR/Cas9 (*SI Appendix*, Fig. 2*B*) decreased the release of EVs, as quantified by total number of particles (*SI Appendix*, Fig. 2*C*), and signal for all the EV-specific surface markers detected by the bead-based multiplex assay (*SI Appendix*, Fig. 2*D*). Incubation of monocytes with the EV-R fraction derived from Rab11-depleted cells led to a lower number of total recovered cells (*SI Appendix*, Fig. 2*E*) and of $CD206^+CD163^+$ cells when compared to monocytes exposed to the EV-R fraction obtained from equal number of control cells, whereas the EV-P fractions of wild-type and Rab11 knockout cells led to similar number of $CD206^+CD163^+$ cells (Fig. 2*F*). Collectively, these results demonstrate that both MDA-MB-231-derived EVs and the soluble factors fraction, poor in EVs, can trigger the differentiation of monocytes toward $CD206^+CD163^+$ macrophages, although the resulting macrophages display different phenotypes.

CSF-1 Exposed on TNBC-Derived EVs Is Required for Macrophage Differentiation. EVs can carry various cytokines as part of their internal cargo or in association with their surface (26). We thus assessed the presence in SEC fractions of cytokines known to be secreted by tumor cells and to potentially affect monocyte fate. Like IL-6 and IL-8 shown in Fig. 1*D*, G-CSF (*CSF3* gene), GM-CSF, and CCL2 were absent in EV-R fractions (Fig. 3*A*). By contrast, CSF-1 was detected both in EV-R and in EV-P fractions. This observation is consistent with the fact that CSF-1 is synthesized as a transmembrane protein and is subsequently cleaved to release the soluble form (27). To determine whether CSF-1 is physically associated with EVs, we isolated EVs by pull-down using beads coated with antibodies against tetraspanins (TSPs) CD9, CD63, and CD81 (PanEVs) (*SI Appendix*, Fig. 3*A*). A total of 30–40% of CSF-1 found in the EV-R is pulled-down together with TSPs-positive EVs (Fig. 3*B*). To confirm the presence of CSF-1 on the surface of

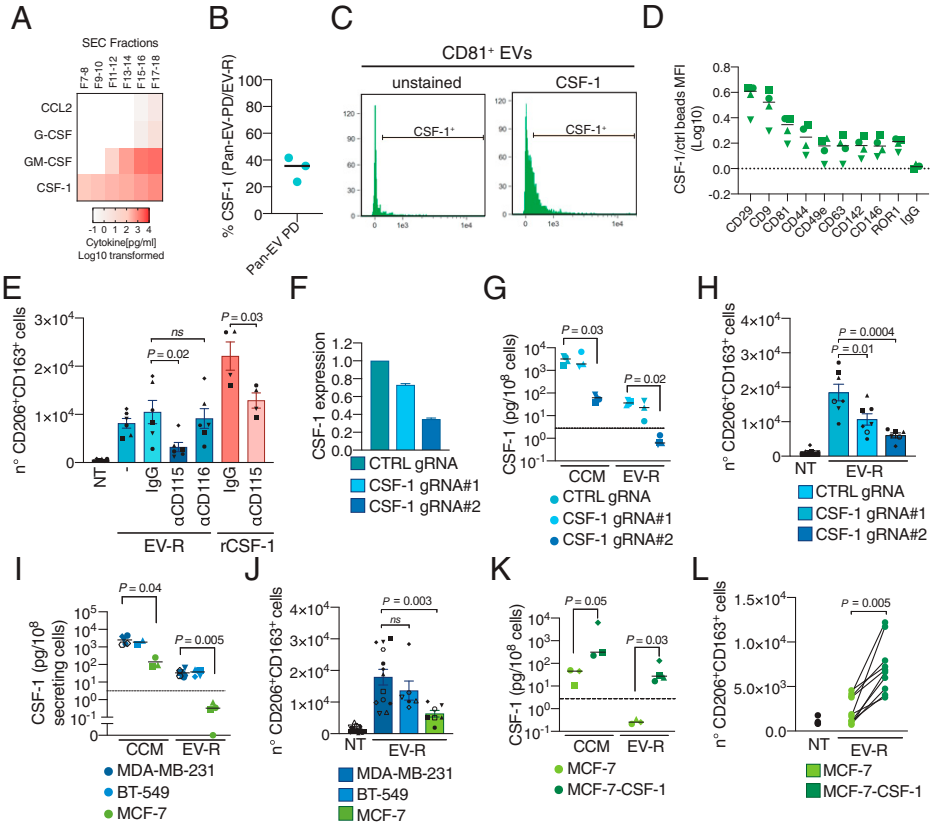

Fig. 3. EVs from TNBC MDA-MB-231 and BT-549 cells but not from luminal MCF-7 cells expose CSF-1 which is required for mo-macs induction. (*A*) Quantification of cytokines present in pooled SEC fractions from MDA-MB-231 cells measured by flow cytometry bead-based assays. Representative of two independent EV isolations. (*B*) Recovery of CSF-1 on MDA-MB-231 EVs by pull-down with anti-CD9, anti-CD81, and anti-CD63 (Pan-EV). (*C*) Presence of CSF-1 on lipid dye positive (membright 488) EVs measured by imaging flow cytometry (ImageStream-X). (*D*) MACSPlexExo analysis of MDA-MB-231 EV-R fractions, developed using a fluorescently coupled antibody against CSF-1. (*E*) Quantification of $CD206^+CD163^+$ live macrophages on day 5 of culture of monocytes with MDA-MB-231 EV-R in the presence of blocking antibodies against CSF-1 Receptor (CD115) or GM-CSF Receptor (CD116) molecules. Each individual donor is shown ($n = 6$). Results shown represent mean ± SEM (*F*) mRNA levels of *CSF1* measured by RT-qPCR in MDA-MB-231 cells transduced with CRISPR/Cas9 lentivectors coding for control gRNA or two gRNA against *CSF1* ($n = 3$, one representative experiment is shown). (*G*) CSF-1 levels in CCM or pooled EV-R fractions from MDA-MB-231 deleted for *CSF1* as indicated. Quantification done on independent EV isolations is shown. (*H*) Number of live $CD163^+CD206^+$ mo-macs obtained upon 5-d culture of purified $CD14^+$ monocytes from healthy donors with EV-R fractions from equal number of secreting control or *CSF1*-deleted MDA-MB-231 cells. Each individual donor is shown ($n = 7$). (*I*) CSF-1 levels in CCM or pooled EV-R fractions from MDA-MB-231, BT-549, and MCF-7 cells. Quantification done on independent EV isolations is shown. (*J*) $CD206^+CD163^+$-positive cells recovered after 5 d or culture of equal amounts of proteins from pooled EV-R fractions from MDA-MB-231, BT-549, or MCF-7 cells with freshly isolated $CD14^+$ monocytes from healthy donors. (*K*) CSF-1 levels in CCM or pooled EV-R fractions from MCF-7 wild-type cells or MCF-7 overexpressing the full-length CSF-1 protein. Quantification done on independent EV isolations is shown. (*L*) EVs from control MCF-7 cells or MCF-7 expressing full-length CSF-1 were incubated with $CD14^+$ cells for 5 d and the number of $CD206^+CD163^+$ cells at the end of the culture is indicated. Comparison between groups was performed by two-tailed, Wilcoxon test. *P* values ≤ 0.05 were considered significant and are indicated for each comparison. Each individual donor is shown. Results shown represent mean ± SEM.

EVs, we analyzed them by imaging flow cytometry (28) (*SI Appendix*, Fig. 3*B*) after labeling with Membright-488 (29), a fluorescent probe that efficiently stains EV membranes (30). Using a combination of fluorochrome-conjugated antibodies against CSF-1 and CD81, we observed that ~40% of $CD81^+$ EVs were positive for CSF-1 (Fig. 3*C* and *SI Appendix*, Fig. 3*C*), while no events positive for both markers were detected in the absence of EVs (*SI Appendix*, Fig. 3*D*). To investigate whether other surface markers may be present on CSF-1-positive EVs, we analyzed the EV-R fraction by the multiplex flow cytometry bead-based assay, replacing the anti-TSPs detection antibodies by an antibody against CSF-1 (Fig. 3*D*). In addition to CD9- and CD81-EVs, we observed that CD29-containing EVs were positive for CSF-1 and, to a lesser extent, CD44-, CD49e-, CD63-, CD142-, CD146-, and ROR1-containing EVs as well, when compared to the isotype control (Fig. 3*D*). Therefore, we conclude that MDA-MB-231-derived EVs transport CSF-1 on their surface.

CSF-1 acts through the cell surface receptor (CD115/CSF-1R), promoting the proliferation, differentiation, and survival of macrophages and their bone marrow progenitors. Given the presence of CSF-1 on the surface of MDA-MB-231-derived EVs and the striking similarity in the CD163/CD206 ratios between EV-R-mo-macs- and rCSF-1-treated cells (Fig. 2*C*), we reasoned that CSF-1 could be, at least in part, mediating EV-induced differentiation of macrophages. To test this hypothesis, we preincubated monocytes with blocking antibodies against CSF-1R (CD115) or GM-CSFR (CD116) before treating them with EV-R fractions. Impairment of CSF-1 signaling dramatically reduced the number of total live cells (*SI Appendix*, Fig. 3*E*) and of $CD206^+CD163^+$ cells recovered at the end of the culture when compared to IgG controls, while, as expected, blocking the receptor for GM-CSF did not affect monocyte survival nor differentiation (Fig. 3*E*). To directly test the role of tumor CSF-1 in EV-mediated monocyte differentiation, we depleted CSF-1 in MDA-MB-231 cells by CRISPR/Cas9 based on two guide RNAs (gRNAs) inducing mild (gRNA#1) or strong (gRNA#2) depletion (Fig. 3*F*). Consistently, the rate of *CSF1*-deletion correlated well with the levels of CSF-1 secreted into the supernatant and associated to EVs (Fig. 3*G*). Furthermore, deletion of *CSF1* decreased the EV-R-induced mo-macs differentiation (Fig. 3*H*) and survival (*SI Appendix*, Fig. 3*F*). Combined, our results obtained using blocking antibodies and gene-editing-based deletion demonstrates that CSF-1 signaling is required for monocyte differentiation induced by MDA-MB-231-derived EVs.

We then addressed whether EVs from other breast cancer cell lines carried CSF-1 and induced mo-macs differentiation as do MDA-MB-231 EVs. We first looked at the expression of CSF-1 in different breast cancer cell lines within the CCLE database that we classified into one of the four breast cancer subtypes (luminal A, luminal B, HER2, and basal/TNBC) according to the literature (31) (*SI Appendix*, Fig. 3*G*). Most of the cell lines with high CSF-1 expression were of basal origin, including MDA-MB-231 cells that are among the highest expressers of CSF-1 mRNA (*SI Appendix*, Fig. 3 *G* and *H*). We chose another TNBC cell line with high level of CSF-1, BT-549, and a luminal A cell line, MCF-7, with low CSF-1 expression. The three cell lines analyzed released a similar amount of EVs (*SI Appendix*, Fig. 3*I*). As observed for MDA-MB-231, BT-549 EVs were also positive for CSF-1, while EVs from MCF-7, which released significantly lower amounts of CSF-1 in accordance with the RNA sequencing (RNA-seq) data, contained no detectable levels of the protein (Fig. 3*I*). MCF-7 EVs induced significantly lower numbers of mo-macs when compared to EVs produced by the two TNBC cell lines analyzed (Fig. 3*J* and *SI Appendix*, Fig. 3*J*), similarly to the results obtained upon CSF-1 deletion. By contrast, when we overexpressed CSF-1 on MCF-7 cells, the protein was released in higher amounts in the conditioned medium and was present on EVs (Fig. 3*K*), which promoted increased mo-macs differentiation (Fig. 3*L* and *SI Appendix*, Fig. 3*K*). Collectively, these results indicate that EVs from cells with high CSF-1 expression, which seems to be a feature of TNBC when compared to luminal cell lines, display CSF-1 molecules on their surface which are necessary for the EV-dependent promotion of mo-macs differentiation.

EVs Released by TNBC Promote an Interferon Response in Macrophages. Considering the findings that CSF-1-containing EV-R and EV-P fractions induced mo-macs with different phenotypes (Fig. 2 *C* and *D*), we decided to establish the mo-macs transcriptome profiles, to better understand their similarities and differences. We performed RNA-seq on mo-macs differentiated by equal quantities of CSF-1 on EV-R fraction or EV-P fraction (0.02 ng/mL) and compared them to the in vitro mo-macs generated with rCSF-1 (100 ng/mL). In addition, we decided to treat monocytes with the same amounts of CSF-1 in the CCM, to obtain macrophages stimulated both with soluble factors and EVs (Fig. 4*A*). We analyzed the overall transcriptomic data by identifying genes displaying a significant differential expression between each pair of conditions (adjusted P value <0.01 and log2 fold change >0.5), and performing a principal component analysis (PCA). Despite some similarities in the level of surface markers among EV-R- and EV-P-mo-macs (*SI Appendix*, Fig. 2*C*), they grouped separately in the PCA (Fig. 4*B*), revealing functionally distinct outcomes on mo-macs differentiation. Using K-means clustering of the differentially expressed genes, we identified seven sets of genes (Fig. 4*C* and Dataset S1). Clusters 7, 6, 5, and 4 were specific for CCM-mo-macs, CSF-1-mo-macs, EV-R-mo-macs, and EV-P-mo-macs, respectively. By contrast, clusters 2, 3, and 1 contained genes enriched in cells exposed to two different treatments: EV-R and EV-P for cluster 2, rCSF-1 and EV-R for cluster 3, and EV-P and CCM for cluster 1. Gene ontology enrichment analysis (GOEA) revealed that enriched terms in EV-R-mo-macs were associated with cytokine-signaling pathways, in particular to those induced by type II (IFN-γ) and type I interferon (IFN), lymphocyte activation, and innate immune response. Conversely, EV-P-mo-macs GO-enriched terms related to neutrophil-mediated immunity and metabolic processes (Fig. 4*D*). Two different activation states are proposed in TAMs: proinflammatory M1 macrophages, which are thought to oppose tumor progression, and M2 macrophages that promote tumor growth (32). This polarization model applies to activation states of in vitro generated macrophages; however, its applicability to macrophages found in the tumor microenvironment, where cells were shown to coexpress both M1 and M2 associated genes, remains controversial (2). Numerous immunostimulatory genes associated with M1 macrophages (2) were found in the EV-R-mo-macs cluster 5, such as *CXCL9*, *CXCL10*, and *CXCL11*, *FCGR1A*, *IDO1*, *KYNU*, *PTPRC* (CD45), and *LY75* (CD205). However, this cluster also comprised several genes previously associated with M2 macrophages—*PDCD1LG2* (PD-L2), *CD274* (PD-L1), and *CCL20*. Therefore, we evaluated the expression of the M1 and M2 signatures within the different groups of mo-macs. Consistent with the observed presence of several genes associated with the M1 signature in the EV-R-mo-macs cluster 5, these

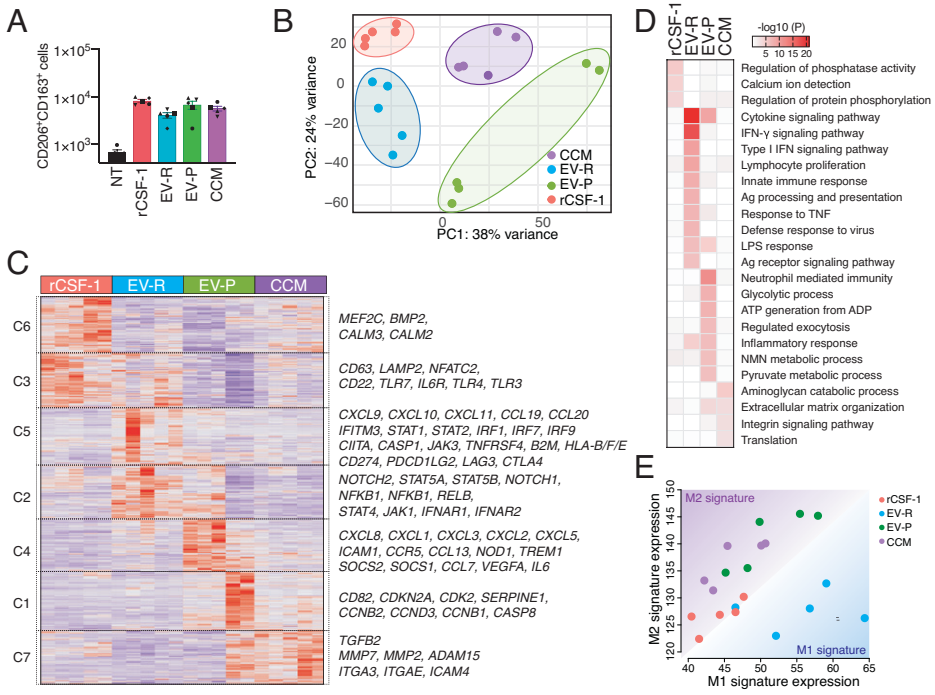

Fig. 4. Mo-macs induced upon MDA-MB-231 EVs treatment express IFN response genes and are enriched in M1 signature. (*A*) Number of live $CD206^{+}CD163^{+}$ cells obtained after 5 d of culture of $CD14^{+}$ monocytes with equal amounts of CSF-1 on EV-R, EV-P, or CCM (0.02 ng/mL) or with rCSF-1 (100 ng/mL) ($n = 5$). (*B*) Transcriptomic analysis of mo-macrophages differentiated as indicated in (*A*). Principal component analysis on the 5,000 most variant genes. (*C*) K-means clustering of differentially expressed genes. (*D*) Gene Ontology analysis of biological processes enriched in the clusters specific for each type of macrophage (cluster 5 for EV-R-mo-macs, cluster 4 for EV-P-mo-macs, cluster 6 for CSF-1-mo-macs, and cluster 7 for CCM-mo-macs). (*E*) Scatter plot of normalized mean expression of M1 and M2 signatures per group.

mo-macs had the highest expression of the M1 signature while they were low in the M2 signature (Fig. 4*E*). Conversely, EV-P-mo-macs were high in the M2 signature (2), but were likewise high in the M1 signature in some replicates (Fig. 4*E*). CCM-mo-macs were slightly higher in M2 signature, and CSF-1-mo-MACS expressed equal low levels of both M1 and M2 signatures.

These findings support the recent idea that macrophage activation in the tumor microenvironment does not necessarily behave as discrete states, since both M1 and M2 associated genes can be induced by tumor-secreted factors. However, we have observed that depending on the nature of the stimuli, EVs or soluble factors or the combination of both, the balance toward one state of activation or the other can be slightly shifted. In addition to the increased PD-L1 and PD-L2 expression in EV-R-mo-macs, other immune checkpoint genes were specifically expressed in these cells, such as *CTLA4* and *LAG3* (Fig. 4*C* and Dataset S1). Overall, our results demonstrate that tumor cells secrete both EVs and soluble factors that impact differently on monocytes, promoting the generation of distinct macrophage subtypes characterized by their unique transcriptional signatures.

EVs from TNBC Activate IFN Response Genes in Monocytes Partly through the cGAS/STING Pathway. EVs can carry nucleic acids and proteins that can act as danger-associated molecular patterns (DAMPs) in recipient cells, triggering a rapid activation of signaling pathways that promote inflammation (17). A characteristic response to the detection of DAMPs is the secretion of elevated levels of cytokines, especially IFN type I and the induction of IFN stimulated genes (ISGs). Our RNA-seq data indicated the activation of both type I and II IFN pathway in EV-R-mo-macs (Fig. 4*D*). To study which genes regulated by IFN were induced upon EV treatment, we queried genes in the cluster 5 (i.e., specific for EV-R-mo-macs) in a database of IFN-regulated genes, Interferome (http://www.interferome.org/) (33), and analyzed their expression across the different RNA-seq samples (Fig. 5*A*). We observed that the IFN type I response genes coding for the chemokines CXCL9 and CXCL10, and the transcription factor IRF7, were highly expressed in EV-R-mo-macs at the RNA level. Thus, we validated these findings by measuring at the protein level either the secretion of these anti-viral induced ISGs into the supernatant of the mo-macs culture (Fig. 5*B*) or the intracellular expression of IRF7 by FACS (Fig. 5*C*). We observed a stronger induction of CXCL9 and CXCL10 secretion by EV-R than by any other treatments (rCSF1, EV-P, and CCM), and a specific induction of IRF7 by EV-R and CCM, whereas neither rCSF1 nor EV-P induced its expression.

To better understand what drives the observed IFN response, we evaluated which pathways within monocytes were necessary for the EV-R-induction of ISGs. Activation of the cGAS/STING cytoplasmic DNA sensing pathway results in robust production of type I IFN (34). STING is activated upon binding of its ligand, the second messenger 2′3′-cyclic GMP-AMP (cGAMP) that is synthesized by the enzyme cyclic-GMP-AMP synthase (cGAS) in response to cytosolic double stranded (ds)DNA (35). Since nucleic acids contained within EVs have been proposed to trigger this pathway in recipient cells (36–38), we evaluated whether STING was required for the EV-R-induced ISG response in mo-macs. To assess this, we preincubated monocytes with a pharmacological inhibitor of STING (H-151) before the 5-d treatment with MDA-MB-231-derived EVs or rCSF-1 and analyzed both macrophage differentiation and cytokine secretion. Although not statistically different, the number of $CD206^{+}CD163^{+}$ cells recovered at

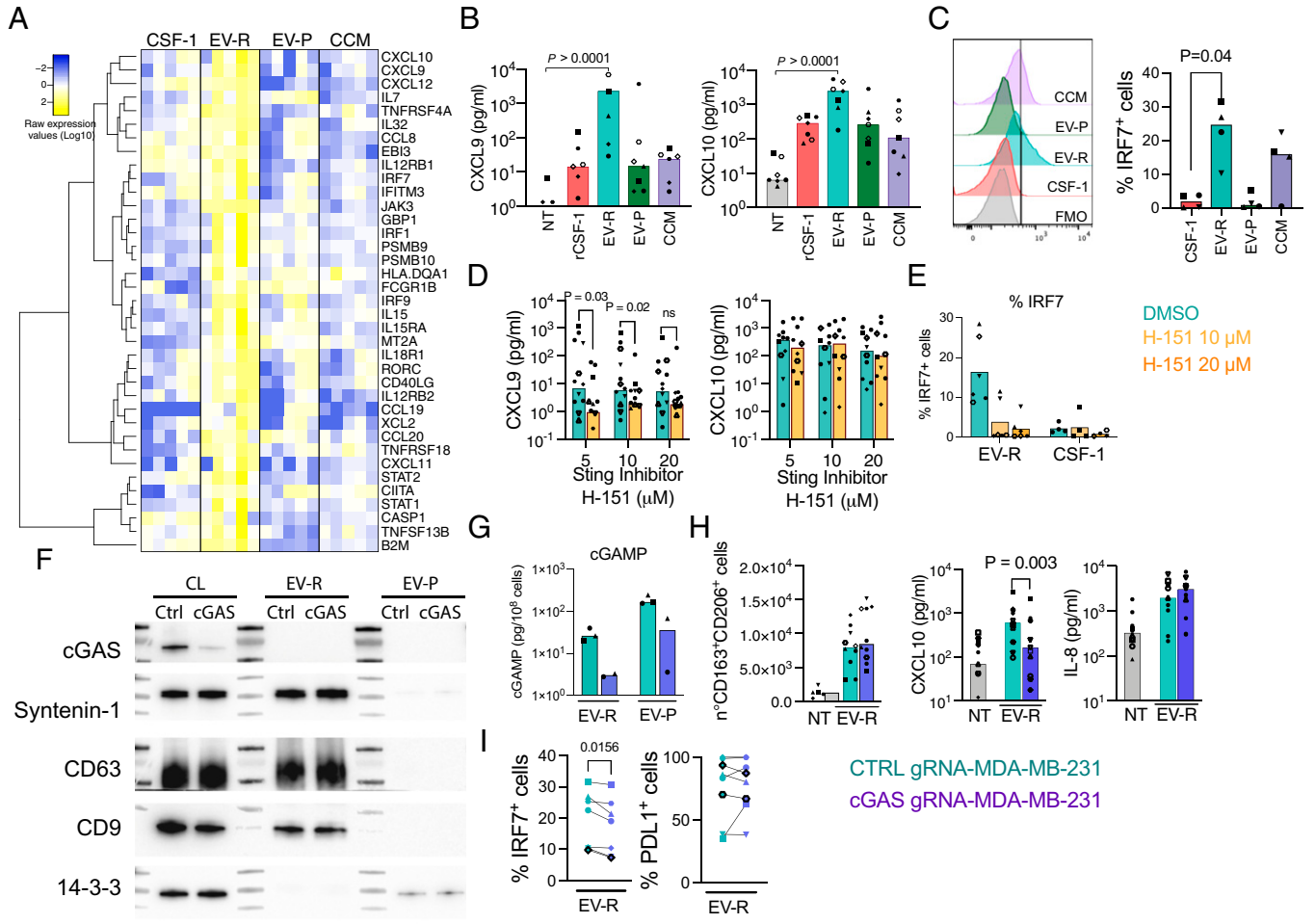

Fig. 5. Role of STING in recipient monocytes and cGAS in EV-producing tumor cells in IFN response in EV-R-mo-macs. (*A*) Heat map of ISGs present in cluster 5 from RNA-seq K-means clustering analysis (EV-R-mo-macs specific cluster) identified as IFN-related in the GO biological processes analysis. (*B*) Quantification of CXCL9 and CXCL10 present at day 5 in the supernatant of monocytes treated with rCSF-1, EV-R, EV-P, or CCM was evaluated by cytometric bead array (CBA). (*C*) Expression of IRF7 (*Left*) and percentage of IRF7 positive cells (*Right*) in monocytes treated for 5 d with rCSF-1, EV-R, EV-P, or CCM, measured by intracellular staining. (*D*) Quantification of CXCL9 (*Left*) and CXCL10 (*Right*) present at day 5 in the supernatant of monocytes treated with EV-R with or without STING inhibitor was evaluated by CBA. (*E*) Percentage of IRF7 positive $CD163^+CD206^+$ cells at day 5 in culture of monocytes treated with EV-R or rCSF1 with or without STING inhibitor. (*F*) WB for cGAS and EV-associated proteins done on cell lysates (CL), EV-R, and EV-P fractions of MDA-MB-231-SCR-gRNA (Ctrl) or MDA-MB-231-cGAS-gRNA (cGAS). (*G*) Measurement of cGAMP levels in EV-R and EV-P SEC fractions of MDA-MB-231 control cells or cGAS-deleted cells. (*H*) EV-R from an equal amount of MDA-MB-231 control (CTRL gRNA) or cGAS-deleted (cGAS gRNA) cells were incubated with $CD14^+$ monocytes for 5 d. At the end of the culture the number of $CD163^+CD206^+$ cells was evaluated by FACS (*Left*) and secretion of CXCL10 (*Middle*) and IL-8 (*Right*) was measured by CBA. (*I*) Percentage of IRF7 and PDL1 positive cells among $CD163^+CD206^+$ at the end of the culture of monocytes treated as in (*H*) with EVs from control cells or cGAS-deleted cells. For (*D*), (*E*), (*H*), and (*I*), comparison between groups was performed by two-tailed, Wilcoxon test. *P* values ≤0.05 were considered significant and are indicated for each comparison. For (*A*) and (*B*), Friedman test for comparison among groups was performed.

the end of the culture trended lower at the highest dose of STING inhibitor for the EV-R treated cells (*SI Appendix*, Fig. 4*A*). This was explained by a reduced expression of CD163 upon inhibitor treatment, while CD206 levels remained unchanged (*SI Appendix*, Fig. 4*B*), and the number of live cells at the end of the culture tended to increase in STING-inhibited cells, although not significantly (*SI Appendix*, Fig. 4*C*). Contrary to the differences observed on EV-R treated monocytes, CSF-1-induced macrophage differentiation was not affected upon STING inhibition (*SI Appendix*, Fig. 4 *A–C*). These observations indicate that STING activation is necessary for CD163 induction by EVs. In addition, cells incubated with the STING inhibitor produced lower levels of CXCL9 upon EV treatment, whereas no significant changes were observed for CXCL10, a chemokine also highly sensitive to nuclear factor κB activation, in addition to IFN (39) (Fig. 5*D*). Up-regulation of IRF7 expression was observed upon EV-R (but not upon CSF-1) treatment, and it was abrogated in STING-inhibited cells, suggesting that this gene is specifically induced by the STING pathway upon EV-R exposure (Fig. 5*E*). To further validate these findings, we depleted STING in the monocytic cell line THP-1 by CRISPR/Cas9 (*SI Appendix*, Fig. 4*D*). As previously observed for freshly isolated monocytes, chemokine secretion was induced upon treatment of THP-1 cells with MDA-MB-231-EV-R (*SI Appendix*, Fig. 4*E*). However, in THP-1, secretion of both CXCL10 and CXCL9 was significantly decreased in STING-depleted cells (*SI Appendix*, Fig. 4*F*). Moreover, the IFN-inducible genes *SIGLEC1* and *IRF7* were highly expressed upon EV treatment of control cells but not of STING-depleted THP-1 cells, which expressed at basal level lower levels of these proteins (*SI Appendix*, Fig. 4*G*). In parallel, treatment of THP-1 control cells by rCSF1 did not induce SIGLEC1 or IRF7 expression as did EV-R fractions (*SI Appendix*, Fig. 4*G*). Thus, STING in THP1 recipient cells is necessary for EVs to induce the IFN response, and secretion of proinflammatory chemokines together with a fully differentiated

macrophage phenotype, whereas in primary monocytes, STING is required for induction by EVs of some inflammatory genes (e.g., CXCL9 and IRF7), but not all (e.g., CXCL10). Plausible explanations of this STING-dependent response would be that either dsDNA within EVs is transferred to recipient cell cytosol and directly activates cGAS or that cGAMP is being transferred within EVs and is directly activating STING in monocytes. Cytosolic cGAMP was shown to spread to bystander cells through gap junctions (40) or through budding viral particles (41, 42). Tumor cells, including MDA-MB-231 cells (43), produce and secrete high quantities of cGAMP, which was proposed to be transferred to host nontumor cells where it triggers STING, resulting in type I IFN production and induction of anti-tumor responses in mouse models (44–46). Thus, to explore the possible transport of cGAMP through EVs, we measured cGAMP levels in the different SEC fractions of conditioned medium and deleted cGAS in tumor cells by CRISPR/Cas9 (Fig. 5*F*) to evaluate whether EVs from these cells induced an ISG response in monocytes. We confirmed previous work (43), showing that cGAMP can be released by MDA-MB-231 tumor cells (Fig. 5*G*). A majority of cGAMP was present in the EV-P fractions, but a detectable portion was found in EV-R fractions with a major decrease upon cGAS deletion in EV-secreting tumor cells (Fig. 5*G*). cGAS-deleted cells released an equal amount of EVs when compared to wild-type MDA-MB-231 cells (*SI Appendix*, Fig. 4*H*), with similar protein marker profile (Fig. 5*F*) and EV-associated CSF-1 (*SI Appendix*, Fig. 4*I*). EV-R from cGAS-deleted MDA-MB-231 cells had similar abilities to promote survival (*SI Appendix*, Fig. 4*J*) and to generate $CD206^{+}CD163^{+}$ mo-macs when compared to controls (Fig. 5 *H*, *Left Panel*). However, these EVs were unable to induce CXCL10 secretion (Fig. 5 *H*, *Middle Panel*), while the induction of IL-8, an IFN-independent cytokine, remained unaltered (Fig. 5 *H*, *Right Panel*). In addition, EV-R from cGAS-deleted cells induced slightly lower levels of IRF7 when compared to control EVs, while PDL1 levels remained unaltered (Fig. 5*I*). Similarly, when stimulating THP-1 cells, EVs from cGAS-deleted cells induced lower levels of IRF7 and Siglec-1 (*SI Appendix*, Fig. 4*K*) and of CXCL10 secretion (*SI Appendix*, Fig. 4*L*) than wild-type EVs. Altogether, these results demonstrate that cGAS-dependent production of cGAMP and its packaging in EVs contribute to the induction of the ISG response triggered by EVs in myeloid cells. Our results, however, do not exclude that, in addition to cGAMP, other cargoes of EVs, including cGAS-independent ones, may also participate in induction of ISG genes, in both STING-dependent and -independent manners.

Human TNBC Release CSF-1-Containing EVs and Are Infiltrated with Macrophages Enriched in the EV-R-mo-macs Signature. To investigate the clinical significance of CSF-1-containing EVs in TNBC and their ability to promote macrophage differentiation, we first evaluated whether EVs containing CSF-1 were released ex vivo by human tumors. EVs were concentrated from conditioned medium obtained upon overnight culture of resected primary breast tumor or juxta-tumor (noninvolved) explants (Fig. 6*A*). We measured CSF-1 in conditioned medium and observed that similar levels of total secreted CSF-1 were observed for TNBC and luminal tumor samples, while low levels were found for the juxta-tumor tissue (Fig. 6 *B*, *Left Panel*). Strikingly, EVs from TNBC tumors contained detectable levels of CSF-1 when compared to luminal tumor-derived EVs, whose measurements were always close to the detection limit of the assay (Fig. 6 *B*, *Right Panel*). To assess whether mo-macs cells obtained in our in vitro system resembled cells present in the tumor microenvironment, we selected the most-deregulated genes (log2 fold change >2 when compared against all the groups) from the EV-R- or EV-P-mo-macs sets of genes (clusters 5 and 4, respectively, Fig. 4*C* and Dataset S1) to generate an EV-R (Fig. 6*C* and Dataset S2) and an EV-P gene signature (Dataset S2), which we used for further comparison with different in vivo RNA expression datasets. First, we analyzed in-house generated single-cell RNA-seq (scRNA-seq) data of tumor-infiltrating $HLA\text{-}DR^{+}CD11c^{+}$ sorted cells from early-stage treatment-naive TNBC patients (*SI Appendix*). The scRNA-seq dataset was analyzed considering only the monocyte and macrophage clusters (Fig. 6*D*). Strikingly, the EV-R gene signature was expressed in specific clusters from myeloid cells infiltrating TNBCs in the scRNA-seq dataset (Fig. 6 *D*, *Middle Panel*). Visualization of the EV-R signature on the scRNA-seq uniform manifold approximation and projection (UMAP) revealed that EV-R-mo-macs mainly resembled a cluster identified as early-macrophages responsive to IFN (Early-MAC-cluster 4) (Fig. 6 *D*, *Left Panel*). These results highlight that the EV-R-induced response is found in an ex vivo dataset, suggesting that TNBC-derived EVs can contribute to shaping the phenotype of cells present in human cancers. Moreover, genes of the EV-P signature were highlighted in the regions of the UMAP representing a cluster of monocytes (cluster 7) and an early macrophage cluster 0 (Fig. 6 *D*, *Right Panel*). Altogether, these results demonstrate that EV-R-mo-macs or EV-P-mo-macs generated in vitro have similar features to different monocyte-derived macrophages subpopulations present in human tumors. We next investigated whether the EV-R-mo-macs and EV-P-mo-macs signatures were associated with clinical outcome in the Molecular Taxonomy of Breast Cancer International Consortium (METABRIC) cohort (47). We observed a higher expression of the EV-R-mo-macs signature in TNBC when compared to luminal or HER2 subtypes, while the EV-P-mo-macs signature was slightly higher in luminal subset (Fig. 6*E*). In addition, only the EV-induced signature was correlated with estimated T and natural killer (NK) cell infiltration (2), both for memory, cytotoxic $CD8^{+}$ T cells and exhausted $CD8^{+}$ T cells (48), and core T regulatory cells (49) (Fig. 6*F*). The chemokines associated to the EV-R-mo-macs, CXCL9 and CXCL10, together with CXCL11 (Fig. 5*A*), correlate with the level of tumor-infiltrating lymphocytes in human cancers (50–52), and their secretion by macrophages is required for anti-tumor immune responses following immune checkpoint blockade in breast cancer (53). Thus, we evaluated the ability of macrophage CM to attract T cells in a migration assay. CM from EV-R-mo-macs was able to induce migration of total T cells when compared to medium alone (Fig. 6*G*), indicating that chemokines released by mo-macs upon tumor EV treatment promote T cell migration. Finally, when considering the clinical outcome among TNBC patients, the EV-R-mo-macs signature was significantly associated with an improved survival (Fig. 6 *H*, *Left Panel*) while EV-P-mo-macs signature had no impact (Fig. 6 *H*, *Middle Panel*). The EV-R signature contains only 23 genes of cluster 5 (Fig. 4*C*), and the vast majority (21 genes) are not canonical IFN response genes (Dataset S2). Notably, TNBC patients expressing high level of the canonical IFN signature were not as strongly associated with improved survival as patients expressing high EV-R-mo-macs signature (Fig. 6*H*). Collectively, our results show that TNBCs release CSF-1-exposing EVs that induce monocyte differentiation into a population of macrophages that possess a unique signature associated with better prognosis.

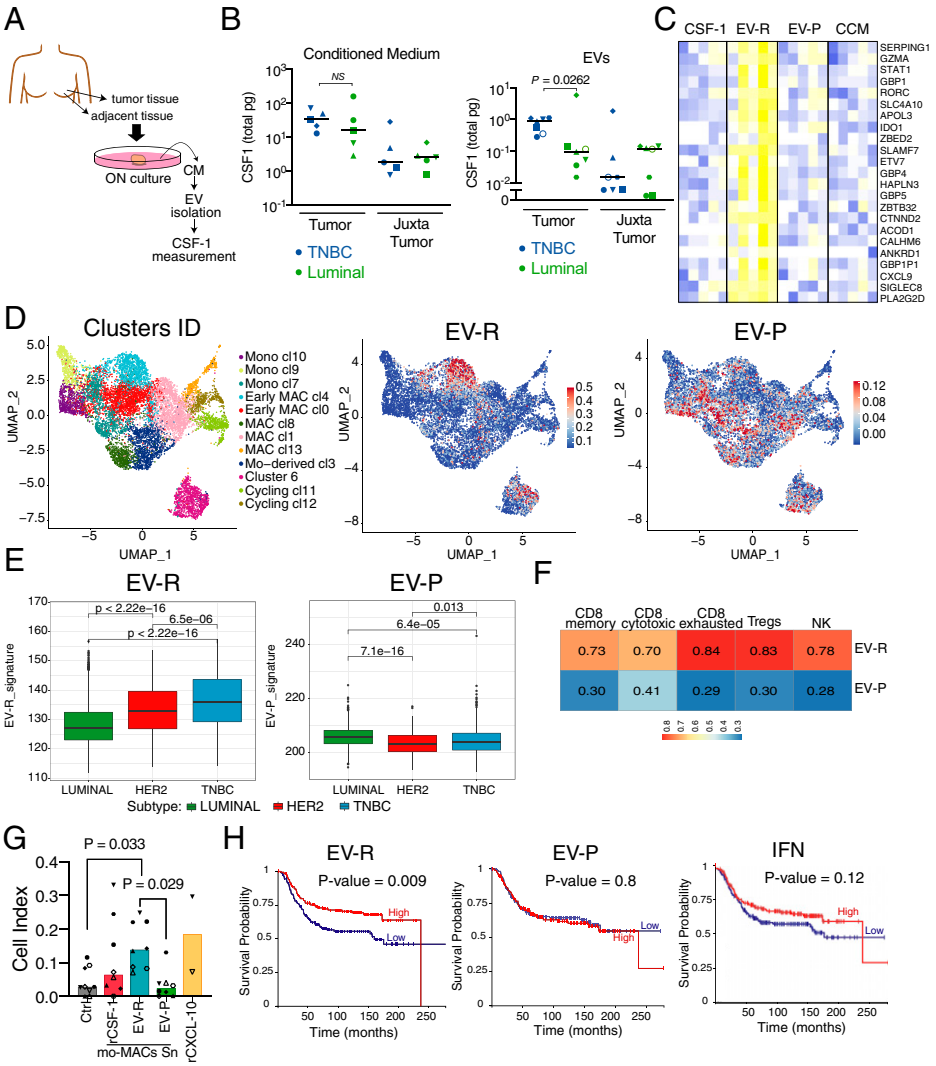

Fig. 6. TNBC human tumors release EVs containing CSF-1 and their infiltration with macs containing an EV-R-mo-macs signature confers them better survival probability. (*A*) Scheme of tissue-explant culture method for EV isolation from paired tumor tissue and juxta-tumor tissue. EVs were isolated from small volumes of prefiltered CM by ultracentrifugation. (*B*) Absolute CSF-1 pg present in 400 μL of conditioned medium as described in (*A*) or in EVs obtained from 400 μL of conditioned medium. (*C*) Heat map of the genes with the strongest up-regulation (log2 fold change >2) in the EV-R-mo-macs when compared to all the other conditions. These 23 genes constitute the EV-R-signature used to analyze RNA from patients' tumor samples. (*D*) Expression of EV-R-mo-macs- or EV-P-mo-macs-enriched genes in TNBC tumor-infiltrating HLA-DR$^+$CD11c$^+$ cells as determined by scRNA-seq. UMAP embedding of single cells as per the original study are shown, with color intensity representing normalized signature expression level. (*Right Panel*) UMAP map of macrophage and monocytes clusters from the HLA-DR$^+$CD11c$^+$cells scRNA-seq analysis from all seven TNBC patients with the identified clusters is shown. Each dot represents a cell, colored by clusters. EV-R and EV-P gene signatures (*E*) EV-R-mo-macs and EV-P-mo-macs signature expression across breast cancer subsets on the METABRIC cohort (Luminal, n = 1,314; Her2, n = 243; TNBC, n = 330). (*F*) Correlation of the EV-R-signature and the EV-P-signature with established signatures for CD8 cytotoxic, CD8 memory, CD8 exhausted, and CD4 T regulatory cells and NK cells in the METABRIC cohort. (*G*) Assay for migration of total T cells using xCELLigence. T cells were seeded in the upper chamber, and supernatant from rCSF-1-mo-macs or EV-R-mo-macs or EV-P-mo-macs or rCXCL10 in the lower chamber of CIM-plates. Migration was evaluated for 24 h. (*H*) Kaplan-Meier curves showing overall survival of TNBC patients from the METABRIC cohort stratified by high (red) and low (blue) expressions of EV-R-mo-macs (*Left*), EV-P-mo-macs (*Middle*), or of a canonical IFN signature (*Right*). Survival curves were compared with the log-rank test (n = 330).

Discussion

In this work, we show that TNBC-released EVs induce monocyte differentiation into a subset of proinflammatory mo-derived macrophages. Our results demonstrate that EVs convey simultaneously multiple messages to target cells, which results in the activation of signaling pathways not provided by soluble messengers signaling individually. The unique association of the macrophage growth factor CSF-1 to EVs in TNBC cooperates with EV molecules to promote the differentiation of macrophages in vitro whose unique signature is found in patients. Moreover, the CSF-1-EV-induced macrophages signature is associated with a favorable patient's clinical condition in TNBC. Our results show that CSF-1, which is synthesized as a membrane-bound precursor (27), is sorted toward EVs and can have different functional features than the classical cleaved soluble form.

Our study uncovers a molecular mechanism of TNBC-EVs effect on macrophages. On the one hand, CSF-1 exposed on the surface of the EVs promotes monocyte survival and differentiation into macrophages. On the other hand, EVs carry other signaling molecules, including (but not only) cGAMP, which activate the STING and other maturation pathways in monocytes, inducing the expression of IFN response genes. The finding that EVs can activate STING in recipient monocytes resulting in the expression of IFN response genes agrees with the mounting evidence that STING activation in cancer leads to IFN production and ISG expression. Several mechanisms of activation have been proposed. On the one hand, tumor DNA

was suggested to be transferred to host immune cells where it could be sensed by cGAS, leading to the activation of STING (54–56). On the other hand, cGAMP can be directly transferred to host immune cells where it triggers STING independently of host cGAS, inducing the secretion of cytokines that enhance NK cell cytotoxicity (46). Upon viral infection, cGAMP transfer had been suggested to occur either via gap junctions (40, 46), through viral particles (41, 42) and transfer via membrane fusion (57). Our work thus highlights EVs as an active component of this cGAMP transfer in vivo but suggests also that other EV components contribute to monocyte activation, in both STING-dependent and STING-independent manners.

The impact of EVs on monocytes resulted in the generation of mo-macs transcriptionally different from those generated upon treatment with tumor-secreted soluble factors poor on EVs or recombinant CSF-1, thus allowing us to determine a unique signature for each macrophage subtype. Macrophages enriched in the EV-R-mo-macs signature were found in a TNBC patients scRNA-seq dataset performed on HLA-DR$^+$ CD11c$^+$ cells, indicating that macrophages with a similar phenotype as those generated in vitro are present in human tumors. Analysis of the METABRIC cohort indicated that the signature associated with EV-R-mo-macs was enriched in TNBC when compared to luminal and HER2 and importantly, was associated with T lymphocytes and NK cells infiltration and a better prognosis in TNBC. These results support previous studies on BC showing that highly infiltrated tumors are associated with good outcomes and responses to chemotherapy (58). For TNBC, our results go in line with the finding of different stratification of immune infiltration in TNBC patients, and the existence of a population of fully inflamed tumors associated with better outcomes characterized by a type I IFN signature, infiltration of effector CD8$^+$ T cells and of proinflammatory macrophages (59, 60). Another recent work described a similar immune-active TNBC subtype defined also by a type I IFN activation, a higher NK and T cell infiltration and also associated with favorable prognosis (60). Importantly, despite the better prognosis, these TNBC tumors have the highest expression of several immune checkpoints such as PD-L1 (59, 60) and the immune modulator IDO-1, and are associated with the highest T regulatory cells infiltration (59). Here, we propose a mechanism consisting of tumor-derived EVs inducing macrophages with high expression of immune checkpoint molecules that secrete high levels of T cell chemoattractant. These TAMs thus display a mixture of the M1- and M2-associated features that were identified by in vitro experimental systems of monocyte differentiation (61, 62), thus confirming recent proposals based on scRNA-seq studies of ex vivo TAMs (2–4), that this simple dichotomy does not apply to the complex context of tissue in general, and tumor in particular, environment.

Whether the EV-induced macrophages found in tumors in vivo are immuno-stimulatory per se will require further experiments. However, our results suggest that these TAMs contribute to a particular local immune landscape, associated with T and NK cell infiltration, which may respond well to immunotherapeutic and chemotherapeutic approaches (63, 64). This observation has important therapeutic implications for TNBC. These tumors are the most aggressive tumors among all the BC subtypes, they have poor clinical outcome when compared to non-TNBC, lack specific therapies, and have higher risk of early relapse. Thus, identifying the subset of patients that do respond to therapy is an unmet challenge. The EV-R-mo-macs signature identified in this work may provide important information to classify patients that will respond well to standard-of-care chemotherapy. In addition to chemotherapy, immunotherapies have arisen as therapeutic options in TNBC (65), since these tumors are highly immunogenic (66), which is reflected by the dense infiltration of immune cells and the intratumoral inflammatory response (67, 68). It would now be interesting to explore whether the EV-R-mo-macs gene expression signature identified in our study could identify patients likely to respond the most efficiently to such immunotherapies.

Materials and Methods

Cell Culture and Transfections. MDA-MB-231 and MCF-7 cells were cultured in Dulbecco's modified Eagle's medium (DMEM-Glutamax, Gibco), with 10% fetal calf serum (FCS, Gibco), 100 U/mL penicillin, and 100 μg/mL streptomycin (Gibco). BT-549 and THP-1 cells were cultured in RPMI-1640-Glutamax medium (Gibco) with penicillin-streptomycin and 10% of FCS. CRISPR/Cas9 modified MDA-MB-231 and MCF-7 cells overexpressing CSF-1 (see *SI Appendix*) were kept in culture in complete medium under antibiotic selection (2 μg/mL puromycin, Thermofisher).

CRISPR/Cas9 Edited Cells. STING KO THP1 cells were established by Cas9/gRNA RNP electroporation using predesigned Alt-R CRISPR-Cas9 crRNAs (IDT technologies, see *SI Appendix*). cGAS KO, CSF-1 KO, or Rab11 KO MDA-MB-231 cells were established by lentiviral-mediated CRISPR/Cas9 method (see *SI Appendix*). The knockout efficiency was evaluated by quantitative reverse transcription PCR (RT-qPCR), Western blotting, and/or LEGENDPlex/ELISA (see *SI Appendix*).

Human Specimens and Processing. Analysis of tumors was performed following relevant national law on protection of people taking part in biomedical research (https://www.sciencedirect.com/topics/medicine-and-dentistry/biomedical-research). Female patients were included in this study and only samples from patients that provided verbal informed consent for tissue donation were processed. Human experimental procedures were approved by the Institutional Review Board and Ethics committee of the Institut Curie Hospital group (approval February 12, 2014) and CNIL (Commission Nationale de l'informatique et des Libertés) (N° approval: 1674356).

Fresh tumor and juxta-tumor tissue were harvested from patients with BC undergoing resection at Institut Curie (69). Surgical residues available after pathological analysis and not required for diagnosis were used. For tumor secretome analysis, once resected, the tissue was placed in CO_2-independent medium (Gibco) within minutes of collection and submitted for downstream processing and analysis. Tissues were cut into 15–20 mg pieces and cultured in one well of a 48-well plate in 250 μL of RPMI GlutaMAX (Gibco) supplemented with 10% FBS (HyClone), 100 U/mL penicillin/streptomycin (Gibco), 1% MEM non-essential amino acids (Gibco), and 1% Pyruvate (Gibco) at 37 °C with 5% CO_2. After 24 h, conditioned media were diluted 1/2 with complete RPMI medium, then filtered with a 0.22 mm filter before storage at −80 °C.

EV Isolation. Cell lines were cultured for 24 h without serum before EVs isolation. The following day concentrated conditioned medium (CCM) was harvested by pelleting cells at 400 × *g* for 10 min at 4 °C. Supernatant was centrifuged at 2,000 × *g* for 20 min at 4 °C to discard 2K pellet and then concentrated on a sterilized Sartorius Centrifugal Filter (MWCO = 100 kDa; VS2061) or Centricon Plus-70 Centrifugal Filter (MWCO = 100 kDa; Millipore). Medium was concentrated to 500 μL and overlaid on 70 nm qEV size-exclusion columns (Izon, SP1) for separation. Twenty-two 500-μL fractions were recovered and analyzed separately or pooled, 7–10 as EV-Rich (EV-R) fraction and 15–22 as EV-Poor (EV-P) fraction. Pooled fractions were then concentrated using 10 KDa cutoff filters (Amicon Ultra-15, Millipore). Protein concentration in EV-R, EV-P, or CCM was measured using Micro-BCA (Thermo Scientific) in the presence of 0.2% SDS.

A total of 200–400 μL of thawed human patients' tumor supernatants were ultracentrifuged at 100,000 × *g* for 30 min in a TLA-45 rotor (Beckman Coulter). Pellets were resuspended in 25 μL of PBS.

EV Characterization.

Western blot. Cell lysates (CL) from 2.10^5 (Fig. 1*C*) or 5.10^4 (Fig. 5*F*) cells, 20 μL of the 500 μL unconcentrated SEC fractions from 400 × 10^6 cells (Fig.

1C) or pooled EV-R and EV-P fractions obtained from 20 × 10^6 cells (Fig. 5F) were analyzed by Western blot in nonreducing conditions (see *SI Appendix*). Membranes were blotted with the following antibodies: mouse anti-human CD63 (clone H5C6, BD Bioscience), mouse anti-human CD9 (clone MM2/57, Millipore), rabbit anti-human 14–3-3 (EPR6380, GeneTex), rat monoclonal anti-human HSC70 (clone 1B5, Enzo Life Sciences), or GP96 (clone 9G10, Enzo Life Sciences). Monoclonal rabbit anti-human syntenin was a gift from P. Zimmermann. Secondary antibodies were purchased from Jackson Immuno-Research.

Bead-based multiplex flow cytometry assay. EV-R fractions were subjected to bead-based multiplex analysis by flow cytometry according to manufacturer instructions using either anti-CD9/CD63/CD81-APC (MACSPlex Exosome Kit, human, Miltenyi) or anti-CSF1-APC (clone 26786, R&D systems, 1/50) for detection (see *SI Appendix*).

Immunoisolation. EV-R fraction from 100 × 10^6 cells was enriched for tetraspanin (CD9, CD63, and CD81)-expressing EVs using Pan Exosome Isolation Kits (Miltenyi Biotech) following manufacturers' instructions. EVs in the flow-through (FT) were recovered by ultracentrifugation at 100,000 × *g* in a TLA-45 rotor for 20 min (Beckman). Pulled-down material (PD) and FT from 10 × 10^6 cells were analyzed by WB for presence of CD9 and CD63. PD from 40–80 × 10^6 cells and FT from 4–8 × 10^6 were used to measure CSF-1 by ELISA.

Imaging flow cytometry. A total of 10^8 EVs were analyzed at the single EV level by imaging flow cytometry (ImageStream X MKII, Amnis/Luminex) following guidelines and principles described in Görgens et al. (28) (see *SI Appendix*), with the following labels: lipid dye MemGlow 488 (Cytoskeleton, Inc), anti-CD81-APC (dilution 1/25) (Clone 5A6, Biolegend), and anti-CSF-1-PE (dilution 1/25) (Clone 26786, R&D Systems). Adequate PBS, unstained, Membright488, CD81, CSF-1 monocolors, and fluorescence minus one (FMOs) EVs controls were performed in parallel.

Monocyte Isolation and Culture. Blood $CD14^+$ monocytes from healthy donors' peripheral blood mononuclear cells (see *SI Appendix*) (2 × 10^5 cells) were cultured for 5 d in complete RPMI medium with 2–4 μg of proteins or equivalent CSF-1 amounts (0.02 ng/mL) from EV-R or EV-P fractions or CCM, or 100 ng/mL of rGM-CSF or 100 ng/mL of rCSF-1 or left untreated. On day 5, supernatants and cells were recovered for analysis. In some experiments, monocytes were pretreated with increasing amounts of STING-specific inhibitor H-151 (Invivogen) or with antibodies against CSF-1R (Bio Techne, MAB3291-SP) or GM-CSFR (Bio Techne, MAB706-SP) for 1 h before the addition of the EV-R fraction.

CTRL or STING KO THP1 cells (5 × 10^5 cells in 100 μL of complete RPMI) were plated with 0.02 ng/mL of CSF-1 or EV-R fractions overnight at 37 °C or left untreated. Cells and supernatants were recovered at 18 h for analysis.

Flow Cytometry. Cells were stained (see *SI Appendix*) with different combinations of the following primary antibodies: HLA-DR/DQ/DP FITC (Clone REA33, Miltenyi), CD163 PE (clone GHI/61, Biolegend), MerTK PeCy7 (clone 590H11G1E3, Biolegend), CD206 Alexa647 (clone 15–2, Biolegend), PDL1 BV421 (clone 29E.2A3, Biolegend), CD16 PE-Cy7 (clone 3G8, Biolegend), CD14 APC-Cy7 (clone 63D3, Biolegend), CD1a PE-Cy5 (clone HI149, BD), anti-CD88 PE (clone S5/1, Biolegend), CD204 APC (clone 7C9C20, Biolegend), CD68 Pe-Vio770 (clone REA835, Miltenyi), SIGLEC1 APC (REA197, Miltenyi), and IRF7 AF488 (12G9A36, Biolegend) or isotype-matched control antibodies. For IRF7 staining, cells were permeabilized with Transcription Factor Staining Buffer (Thermo). Cells were analyzed on a FACSVerse (BD Biosciences) or MACSQuant (Miltenyi) instrument. Data were analyzed with FlowJo (FlowJo LLC)

Morphological Analysis. Cells were subjected to cytospin and colored with May-Grunwald/Giemsa staining (Sigma). Pictures were taken with a CFW-1308C color digital camera (Scion Corporation) on a Leica DM 4000 B microscope.

Cytokines Quantification. CSF-1 and GM-CSF levels in supernatant were measured with LEGENDplex multiplex assay according to manufacturer's instructions. Samples were acquired on a BD FACSverse and analyzed using LEGENDplex software (Biolegend). In some experiments, CSF-1 was measured by ELISA (RAB0098 Sigma-Aldrich) following manufacturer instructions.

Cytometric Bead Array (BD CBA Flex Sets) was used for measuring IL-8, IL-6, G-CSF, CCL2 (MCP1), CXCL10 (IP10), and CXCL9 (MIG) in supernatants according to manufacturer's instructions. Samples were acquired on a BD FACSverse and analyzed with the FCAP Array software.

cGAMP Quantification. 2′3′-cGAMP ELISA Kit (Cayman Chemical) was used for the quantification of cGAMP in EV-R and EV-P fractions according to the manufacturer's instructions, and as described in Jneid et al. (70). After performing the assay, the plate was read at a wavelength of 450 nm. Data were fitted to a 4-parameter sigmoidal curve.

RNA-Seq Library Preparation and Analysis. RNA from 5 × 10^5–10^6 cells mo-macs cells was used for sequencing performed using NovaSeq (Illumina) (100-nt-length reads, paired end) (see *SI Appendix*). Data are accessible through Gene Expression Omnibus series accession number GSE173771. Differential gene expression analysis was performed using *DESeq2* (v1.22.2) (71). Differentially expressed genes between each pair of conditions displaying an adjusted *P* value <0.01 and log2 fold change >0.5 were kept. The union of these genes was used as input for *k*-means clustering of gene expression. The gene ontology analysis was performed using Enrichr (https://maayanlab.cloud/Enrichr/) (72). Enrichments were considered statistically significant if they had *q*-values (i.e., *P*-values adjusted for multiple testing) <0.05. EV-R-genes involved in cytokine mediated signaling pathway (the most significant GO term) were queried in a database of IFN-regulated genes, Interferome (http://www.interferome.org/) (33). Gene signatures for the EV-R-mo-macs and the EV-P-mo-macs groups (Dataset S2) were generated considering the differentially expressed genes displaying an adjusted *P* value <0.01 and log2 fold change >2 when compared among all the other RNA-seq groups. A canonical IFN-gene signature was generated by curation of the literature (kindly provided by L. Niborski, INSERM U932).

scRNA-Seq Analysis. Our in-house study of single-cell RNA-seq on $HLA\text{-}DR^+$ $CD11c^+$ infiltrating tumors from TNBC patients was used (see *SI Appendix* for experimental details; data deposited in Zenodo repository under accession number 5939839). The R package Seurat v3 was used to integrate samples and analyze the datasets. Gene signatures were computed for each cell using AddModuleScore function from Seurat. Briefly, this function calculates for each individual cell the average expression of each gene signature, subtracted by the aggregated expression of control gene sets. The calculations were done on the integrated matrix, setting a parameter of 20 control genes.

Survival Analysis and Correlation Plots in Public Datasets of BC Patients. Bulk analyses were performed using METABRIC cohort (47). Statistical tests were performed using unpaired *t* tests.

Survival plots were generated using XenaBrowser (https://xenabrowser.net/) using METABRIC cohort. High and low cohorts were split in 2 by the median. Correlation plots were computed using the same METABRIC TNBC cohort, using Spearman correlation between gene sum from the signatures, and plotted using pheatmap R package (v1.0.12).

Migration Assay. Migration assays were performed with the xCELLigence RTCA instrument using CIM-16 Transwell plates according to the manufacturer's recommendations (see *SI Appendix*). A total of 40 × 10^5 CD3 T cells in 100 μL of medium with FBS were added in the upper chamber, CM from EV-R-mo-macs, EV-P-mo-macs or CSF-1-mo-macs, or DMEM 10% FBS without or with 100 ng/mL of CXCL10 (negative and positive controls, respectively) were added in the lower chamber. Plates were loaded into the xCELLigence RTCA DP instrument inside a 37 °C incubator for 24 h with readings every 15 min. Data were collected and analyzed by RTCA software.

Data Availability. Bulk RNA sequencing data are openly available in the Gene Expression Omnibus at https://www.ncbi.nlm.nih.gov/geo/query/acc.cgi?acc=GSE173771, reference number GSE173771.

scRNA sequencing data are openly available in the Zenodo repository at https://zenodo.org/record/5939839, reference number 5939839.

ACKNOWLEDGMENTS. We wish to thank Dr. Sebastian Amigorena and Dr. Leticia Niborski (INSERM, U932) for providing tools and helpful discussions, Dr. Jennifer Jones and Dr. Joshua Welsh (NIH/NCI) for helpful discussions, and the Institut Curie NSG and Flow Cytometry facilities for their assistance. This work was supported by Institut Curie (including NCI.NIH-PIC3i-2018 and PIC-TME programs), INSERM, CNRS, the French National Cancer Institute (11548), the French National Research Agency (ANR) (ANR-18-CE13-0017-03, ANR-18-CE15-0008-01,

and ANR-18-CE16-0022-02), Fondation ARC (PGA1 RF20180206962 to C.T. and AAP SIGN'IT2019 to E.R.), H2020- Marie Skłodowska-Curie Innovative Training Network (722148, TRAIN-EV), the National Institute on Drug Abuse (DA040385), French IdEx and LabEx DCBIOL (ANR-10-INSB-04, ANR-10-IDEX-0001-02 PSL, ANR-10-LABX-0038, ANR-11-LABX-0043, and ANR-18-IDEX-0001 Université de Paris), and Fonds Amgen France pour la Science et l'Humain (to E.R.). P.G. was supported by a PhD fellowship from Ligue Nationale contre le Cancer at Université Paris Descartes (Paris V). E.G. was recipient of a post-doctoral fellowship from the Foundation for Medical Research. E.T. was supported by a postdoctoral fellowship abroad from the AIRC (2018/2020-number: 20934).

1. L. Cassetta, J. W. Pollard, Targeting macrophages: Therapeutic approaches in cancer. *Nat. Rev. Drug Discov.* **17**, 887–904 (2018).
2. E. Azizi *et al.*, Single-cell map of diverse immune phenotypes in the breast tumor microenvironment. *Cell* **174**, 1293–1308.e36 (2018).
3. S. Chevrier *et al.*, An immune atlas of clear cell renal cell carcinoma. *Cell* **169**, 736–749.e18 (2017).
4. Y. Lavin *et al.*, Innate immune landscape in early lung adenocarcinoma by paired single-cell analyses. *Cell* **169**, 750–765.e17 (2017).
5. B.-Z. Qian *et al.*, CCL2 recruits inflammatory monocytes to facilitate breast-tumour metastasis. *Nature* **475**, 222–225 (2011).
6. R. A. Franklin *et al.*, The cellular and molecular origin of tumor-associated macrophages. *Science* **344**, 921–925 (2014).
7. C. Goudot *et al.*, Aryl hydrocarbon receptor controls monocyte differentiation into dendritic cells versus macrophages. *Immunity* **47**, 582–596.e6 (2017).
8. L. Cassetta *et al.*, Human tumor-associated macrophage and monocyte transcriptional landscapes reveal cancer-specific reprogramming, biomarkers, and therapeutic targets. *Cancer Cell* **35**, 588–602.e10 (2019).
9. X. Ying *et al.*, Epithelial ovarian cancer-secreted exosomal miR-222-3p induces polarization of tumor-associated macrophages. *Oncotarget* **7**, 43076–43087 (2016).
10. L. Wu *et al.*, Exosomes derived from gastric cancer cells activate NF-κB pathway in macrophages to promote cancer progression. *Tumour Biol.* **37**, 12169–12180 (2016).
11. A. Chow *et al.*, Macrophage immunomodulation by breast cancer-derived exosomes requires Toll-like receptor 2-mediated activation of NF-κB. *Sci. Rep.* **4**, 5750 (2014).
12. F. Haderk *et al.*, Tumor-derived exosomes modulate PD-L1 expression in monocytes. *Sci. Immunol.* **2**, eaah5509 (2017).
13. M. Tkach, C. Théry, Communication by extracellular vesicles: Where we are and where we need to go. *Cell* **164**, 1226–1232 (2016).
14. G. van Niel, G. D'Angelo, G. Raposo, Shedding light on the cell biology of extracellular vesicles. *Nat. Rev. Mol. Cell Biol.* **19**, 213–228 (2018).
15. F. Cocozza, E. Grisard, L. Martin-Jaular, M. Mathieu, C. Théry, SnapShot: Extracellular Vesicles. *Cell* **182**, 262–262.e1 (2020).
16. F. G. Kugeratski, R. Kalluri, Exosomes as mediators of immune regulation and immunotherapy in cancer. *FEBS J.* **288**, 10–35 (2021).
17. P. D. Robbins, A. E. Morelli, Regulation of immune responses by extracellular vesicles. *Nat. Rev. Immunol.* **14**, 195–208 (2014).
18. M. Tkach, J. Kowal, C. Théry, Why the need and how to approach the functional diversity of extracellular vesicles. *Philos. Trans. R. Soc. Lond. B Biol. Sci.* **373**, 20160479 (2018).
19. C. Théry *et al.*, Minimal information for studies of extracellular vesicles 2018 (MISEV2018): A position statement of the International Society for Extracellular Vesicles and update of the MISEV2014 guidelines. *J. Extracell. Vesicles* **7**, 1535750 (2018).
20. S. Shu *et al.*, Purity and yield of melanoma exosomes are dependent on isolation method. *J. Extracell. Vesicles* **9**, 1692401 (2019).
21. D. K. Jeppesen *et al.*, Reassessment of exosome composition. *Cell* **177**, 428–445.e18 (2019).
22. N. Koliha *et al.*, A novel multiplex bead-based platform highlights the diversity of extracellular vesicles. *J. Extracell. Vesicles* **5**, 29975 (2016).
23. J. Xue *et al.*, Transcriptome-based network analysis reveals a spectrum model of human macrophage activation. *Immunity* **40**, 274–288 (2014).
24. A. Savina, M. Vidal, M. I. Colombo, The exosome pathway in K562 cells is regulated by Rab11. *J. Cell Sci.* **115**, 2505–2515 (2002).
25. S. W. Messenger, S. S. Woo, Z. Sun, T. F. J. Martin, A Ca^{2+}-stimulated exosome release pathway in cancer cells is regulated by Munc13-4. *J. Cell Biol.* **217**, 2877–2890 (2018).
26. E. I. Buzás, E. Á. Tóth, B. W. Sódar, K. É. Szabó-Taylor, Molecular interactions at the surface of extracellular vesicles. *Semin. Immunopathol.* **40**, 453–464 (2018).
27. F. J. Pixley, E. R. Stanley, CSF-1 regulation of the wandering macrophage: Complexity in action. *Trends Cell Biol.* **14**, 628–638 (2004).
28. A. Görgens *et al.*, Optimisation of imaging flow cytometry for the analysis of single extracellular vesicles by using fluorescence-tagged vesicles as biological reference material. *J. Extracell. Vesicles* **8**, 1587567 (2019).
29. M. Collot *et al.*, MemBright: A family of fluorescent membrane probes for advanced cellular imaging and neuroscience. *Cell Chem. Biol.* **26**, 600–614.e7 (2019).
30. V. Hyenne *et al.*, Studying the fate of tumor extracellular vesicles at high spatiotemporal resolution using the zebrafish embryo. *Dev. Cell* **48**, 554–572.e7 (2019).
31. X. Dai, H. Cheng, Z. Bai, J. Li, Breast cancer cell line classification and its relevance with breast tumor subtyping. *J. Cancer* **8**, 3131–3141 (2017).
32. A. Mantovani, M. Locati, Tumor-associated macrophages as a paradigm of macrophage plasticity, diversity, and polarization: Lessons and open questions. *Arterioscler. Thromb. Vasc. Biol.* **33**, 1478–1483 (2013).
33. I. Rusinova *et al.*, Interferome v2.0: An updated database of annotated interferon-regulated genes. *Nucleic Acids Res.* **41**, D1040–D1046 (2013).
34. H. Ishikawa, Z. Ma, G. N. Barber, STING regulates intracellular DNA-mediated, type I interferon-dependent innate immunity. *Nature* **461**, 788–792 (2009).
35. J. Wu, Z. J. Chen, Innate immune sensing and signaling of cytosolic nucleic acids. *Annu. Rev. Immunol.* **32**, 461–488 (2014).
36. Y. Kitai *et al.*, DNA-containing exosomes derived from cancer cells treated with topotecan activate a STING-dependent pathway and reinforce antitumor immunity. *J. Immunol.* **198**, 1649–1659 (2017).
37. J. M. Diamond *et al.*, Exosomes shuttle TREX1-sensitive IFN-stimulatory dsDNA from irradiated cancer cells to DCs. *Cancer Immunol. Res.* **6**, 910–920 (2018).
38. A. Takahashi *et al.*, Exosomes maintain cellular homeostasis by excreting harmful DNA from cells. *Nat. Commun.* **8**, 15287 (2017).
39. J. Melchjorsen, L. N. Sørensen, S. R. Paludan, Expression and function of chemokines during viral infections: From molecular mechanisms to in vivo function. *J. Leukoc. Biol.* **74**, 331–343 (2003).
40. A. Ablasser *et al.*, Cell intrinsic immunity spreads to bystander cells via the intercellular transfer of cGAMP. *Nature* **503**, 530–534 (2013).
41. A. Bridgeman *et al.*, Viruses transfer the antiviral second messenger cGAMP between cells. *Science* **349**, 1228–1232 (2015).
42. M. Gentili *et al.*, Transmission of innate immune signaling by packaging of cGAMP in viral particles. *Science* **349**, 1232–1236 (2015).
43. J. A. Carozza *et al.*, Extracellular cGAMP is a cancer cell-produced immunotransmitter involved in radiation-induced anti-cancer immunity. *Nat. Can.* **1**, 184–196 (2020).
44. L. Schadt *et al.*, Cancer-cell-intrinsic cGAS expression mediates tumor immunogenicity. *Cell Rep.* **29**, 1236–1248.e7 (2019).
45. J. Ahn, T. Xia, A. Rabasa Capote, D. Betancourt, G. N. Barber, Extrinsic phagocyte-dependent STING signaling dictates the immunogenicity of dying cells. *Cancer Cell* **33**, 862–873.e5 (2018).
46. A. Marcus *et al.*, Tumor-derived cGAMP triggers a STING-mediated interferon response in non-tumor cells to activate the NK cell response. *Immunity* **49**, 754–763.e4 (2018).
47. C. Curtis *et al.*; METABRIC Group, The genomic and transcriptomic architecture of 2,000 breast tumours reveals novel subgroups. *Nature* **486**, 346–352 (2012).
48. X. Guo *et al.*, Global characterization of T cells in non-small-cell lung cancer by single-cell sequencing. *Nat. Med.* **24**, 978–985 (2018).
49. D. Zemmour *et al.*, Single-cell gene expression reveals a landscape of regulatory T cell phenotypes shaped by the TCR. *Nat. Immunol.* **19**, 291–301 (2018).
50. C. Denkert *et al.*, Tumor-infiltrating lymphocytes and response to neoadjuvant chemotherapy with or without carboplatin in human epidermal growth factor receptor 2-positive and triple-negative primary breast cancers. *J. Clin. Oncol.* **33**, 983–991 (2015).
51. T. J. Zumwalt, M. Arnold, A. Goel, C. R. Boland, Active secretion of CXCL10 and CCL5 from colorectal cancer microenvironments associates with $GranzymeB^+$ $CD8^+$ T-cell infiltration. *Oncotarget* **6**, 2981–2991 (2015).
52. Q. Ding *et al.*, CXCL9: Evidence and contradictions for its role in tumor progression. *Cancer Med.* **5**, 3246–3259 (2016).
53. I. G. House *et al.*, Macrophage-derived CXCL9 and CXCL10 are required for antitumor immune responses following immune checkpoint blockade. *Clin. Cancer Res.* **26**, 487–504 (2020).
54. J. Klarquist *et al.*, STING-mediated DNA sensing promotes antitumor and autoimmune responses to dying cells. *J. Immunol.* **193**, 6124–6134 (2014).
55. T. Ohkuri *et al.*, STING contributes to antiglioma immunity via triggering type I IFN signals in the tumor microenvironment. *Cancer Immunol. Res.* **2**, 1199–1208 (2014).
56. S.-R. Woo *et al.*, STING-dependent cytosolic DNA sensing mediates innate immune recognition of immunogenic tumors. *Immunity* **41**, 830–842 (2014).
57. S. Xu *et al.*, cGAS-mediated innate immunity spreads intercellularly through HIV-1 Env-induced membrane fusion sites. *Cell Host Microbe* **20**, 443–457 (2016).
58. P. Savas *et al.*, Clinical relevance of host immunity in breast cancer: From TILs to the clinic. *Nat. Rev. Clin. Oncol.* **13**, 228–241 (2016).
59. T. Gruosso *et al.*, Spatially distinct tumor immune microenvironments stratify triple-negative breast cancers. *J. Clin. Invest.* **129**, 1785–1800 (2019).
60. S. Romero-Cordoba *et al.*, Decoding immune heterogeneity of triple negative breast cancer and its association with systemic inflammation. *Cancers (Basel)* **11**, E911 (2019).
61. A. Mantovani *et al.*, The chemokine system in diverse forms of macrophage activation and polarization. *Trends Immunol.* **25**, 677–686 (2004).
62. F. O. Martinez, S. Gordon, The M1 and M2 paradigm of macrophage activation: Time for reassessment. *F1000Prime Rep.* **6**, 13 (2014).
63. J. Galon, D. Bruni, Approaches to treat immune hot, altered and cold tumours with combination immunotherapies. *Nat. Rev. Drug Discov.* **18**, 197–218 (2019).
64. J. Li *et al.*, Tumor cell-intrinsic factors underlie heterogeneity of immune cell infiltration and response to immunotherapy. *Immunity* **49**, 178–193.e7 (2018).
65. C. Kang, Y. Y. Syed, Atezolizumab (in combination with nab-paclitaxel): A review in advanced triple-negative breast cancer. *Drugs* **80**, 601–607 (2020).
66. D. Nagarajan, S. E. B. McArdle, Immune landscape of breast cancers. *Biomedicines* **6**, E20 (2018).
67. S. Loi *et al.*, Tumor-infiltrating lymphocytes and prognosis: A pooled individual patient analysis of early-stage triple-negative breast cancers. *J. Clin. Oncol.* **37**, 559–569 (2019).
68. S. Luen, B. Virassamy, P. Savas, R. Salgado, S. Loi, The genomic landscape of breast cancer and its interaction with host immunity. *Breast* **29**, 241–250 (2016).
69. A. Costa *et al.*, Fibroblast heterogeneity and immunosuppressive environment in human breast cancer. *Cancer Cell* **33**, 463–479.e10 (2018).
70. B. Jneid *et al.*, Cellular selectivity of STING stimulation determines priming of anti-tumor T cell responses. bioRxiv [Preprint] (2021). https://doi.org/10.1101/2021.12.01.469893 (Accessed 1 April 2022).
71. M. I. Love, W. Huber, S. Anders, Moderated estimation of fold change and dispersion for RNA-seq data with DESeq2. *Genome Biol.* **15**, 550 (2014).
72. M. V. Kuleshov *et al.*, Enrichr: A comprehensive gene set enrichment analysis web server 2016 update. *Nucleic Acids Res.* **44**, W90–W97 (2016).